Toward high-performance tracking simulation of long-range resistive-wall driven transverse coupled-bunch instabilities

Xin Huang, Tianlong He,* Hongliang Xu,† Weiwei Li, Zhenghe Bai, and Guangyao Feng

National Synchrotron Radiation Laboratory, University of Science and Technology of China, Hefei, Anhui, 230029, China

(Received 7 July 2026; accepted 16 September 2026; published 5 November 2026)

The long-range transverse resistive-wall (RW) wakefield is a key driver of transverse coupled-bunch instabilities in high-current storage rings. Simulating these instabilities accurately is typically time-consuming, because conventional time-domain tracking codes such as `Pelegant` store the turn-by-turn bunch-centroid history and perform discrete convolutions with the wakefield, which poses a bottleneck for long-term tracking. To overcome this limitation, this work reformulates the long-range RW wakefield calculation, converting the explicit history-dependent convolution into a recursive update by representing the wakefield as a sum-of-exponential functions. This approach avoids storing the bunch-centroid history and is well suited to parallel graphics-processing-unit architectures; it has been implemented in the tracking code `STABLE`. Benchmark tests, using parameters of the Hefei Advanced Light Facility (HALF), show that `STABLE` with the proposed method maintains high accuracy in the growth rate while achieving a speedup of at least 2 orders of magnitude over `Pelegant`. Leveraging this computational efficiency, we conduct a systematic study of RW instabilities for HALF, with particular focus on the interplay among filling pattern, chromaticity, and harmonic-cavity bunch lengthening.

DOI: 10.1103/hfw9-6759

I. INTRODUCTION

In high-current storage rings, transverse coupled-bunch instabilities (TCBIs) are important collective effects that can limit the beam current and degrade accelerator performance. The long-range resistive-wall (RW) wakefield is one of the major driving sources of TCBIs. Its contribution has been identified in instability studies of a number of fourth-generation storage-ring light sources [1–7] and is also relevant to existing and future high-current collider rings [8–13]. Therefore, accurate evaluation of RW-driven TCBI is essential for machine design and operation.

Studies of RW-driven TCBI generally rely on two approaches: theoretical analysis and numerical tracking. The simplest theoretical description treats each bunch as a pointlike oscillator [14], reducing the problem to an eigenvalue analysis of coupled-bunch centroids. Sacherer [15] developed a mode expansion method that describes the perturbed beam distribution using orthogonal azimuthal and radial modes to capture chromatic and intrabunch longitudinal effects. While insightful, this framework becomes inadequate at high chromaticity, where intermode coupling is non-negligible. Laclare [16] later simplified the approach by retaining only azimuthal modes and neglecting radial coupling and derived practical growth-rate expressions under mode-coupling approximations. This improved the applicability for large-chromaticity regimes, though it still omitted synchrotron-radiation effects. For arbitrary filling patterns, Bassi *et al.* [17] developed an eigenvalue analysis in which the filling pattern is included through the bunch population in each rf bucket, allowing the zero-chromaticity coupled-bunch eigenvalues and growth rates to be computed for prescribed nonuniform fills. More recently, Lindberg [18] formulated a chromaticity-dependent Vlasov theory in which the nonzero-chromaticity growth rate is obtained from a dispersion relation that uses the zero-chromaticity coupled-bunch eigenvalue and the longitudinal equilibrium distribution as inputs.

However, these theories rely on a number of idealized assumptions and linearized formulations to facilitate analytical derivations, such as linearization of the Vlasov equation [18], reduction of the dynamics to centroid or mode-based descriptions [14], and the use of prescribed stationary equilibrium distributions [17,18]. In addition, chromatic effects are often neglected by assuming zero chromaticity in simplified formulations [17]. For more realistic scenarios—such as arbitrary filling patterns and nonidentical bunch distributions induced by harmonic-cavity bunch lengthening [19]—a fully self-consistent

*Contact author: htlong@ustc.edu.cn
†Contact author: hlxu@ustc.edu.cn

Published by the American Physical Society under the terms of the Creative Commons Attribution 4.0 International license. Further distribution of this work must maintain attribution to the author(s) and the published article's title, journal citation, and DOI.

theoretical treatment becomes exceedingly complicated and often cannot yield analytical results. Numerical tracking addresses these effects more directly by evolving macroparticles turn by turn, yet it is computationally demanding for large-scale parameter scans and long-term simulations. Consequently, improving this computational efficiency is a major motivation for the present work.

Conventional long-range RW wakefield treatments in tracking codes such as `Pelegant` [20,21], `mbtrack2` [22,23], `Xsuite` [24,25], and `CETASim` [26] typically compute the wake kick through a convolution of the wake function with the history of bunch-centroid offsets. Although the convolution can be accelerated by Fourier techniques, storing the turn-by-turn, bunch-by-bunch centroid history significantly increases the computational load and severely degrades the efficiency. For this reason, existing codes do not retain the full centroid history; instead, they commonly adopt a truncated record that keeps only a limited number of previous turns, striking a balance between computational speed and result reliability (e.g., 25 turns for the APS-U storage ring [18]).

The `MuSiC` code [27] takes a different approach and avoids the explicit convolution by fitting the RW wakefield with a set of resonators, thereby eliminating the need to store the per-bunch, per-turn centroid history. In this method, the short-range and long-range parts are fitted simultaneously, and achieving good accuracy typically requires a relatively large number of resonators. Moreover, `MuSiC` evaluates the wake kick on a particle-by-particle basis without parallelization, which limits its computational efficiency. By contrast, the `STABLE` code [28] deliberately separates the short-range and long-range wakefields. The short-range part can be merged with other short-range wake modules at no extra computational cost, while the long-range interaction is handled through a phasor representation [29]. This approach not only avoids storing centroid history but also enables graphics-processing-unit (GPU) acceleration, thereby dramatically improving the computational efficiency.

In light of the above, a straightforward idea is to fit the long-range RW wakefield using multiple resonators so that it can be directly processed by `STABLE` [28,29] for efficient simulation. We have carefully compared the characteristics of resonator wakefields and the long-range RW wakefield: the former decay while oscillating, whereas the latter is purely monotonically decaying. A resonator wake function consists of an exponential damping term and an oscillatory phase-rotation term. Discarding the phase rotation and retaining only the exponential decay—i.e., fitting the long-range RW wakefield with a sum of exponentials—should therefore yield even better fitting performance. Furthermore, like resonator-based representations, the exponential-form wakefield is also suited for GPU acceleration, and the absence of the phase-rotation term further reduces the computational load, leading to a significant boost in efficiency. In this work, we implement this exponential-fitting method in the `STABLE` code and validate it using parameters of the Hefei Advanced Light Facility (HALF) [30] listed in Table I by comparing the results with theoretical predictions and with those from `Pelegant`. We apply this method to perform large-scale parameter scans and systematically study the combined effects of harmonic-cavity bunch lengthening, chromaticity, and filling pattern on the RW-driven TCBI for HALF.

TABLE I. Main parameters of HALF.

Parameter	Symbol	Value
Circumference	C	479.86 m
Beam energy	E_0	2.2 GeV
Nominal beam current	I_0	350 mA
Harmonic number	h	800
Main-cavity voltage	V_{rf}	1.2 MV
Energy loss per turn	U_0	380 keV
Momentum compaction factor	α_c	9.4×10^{-5}
Natural rms bunch length	$\sigma_{\tau 0}$	7.16 ps
Natural energy spread	σ_δ	7.44×10^{-4}
Natural horizontal emittance	ϵ_{x0}	86 pm rad
Betatron tunes	$\nu_{x,y}$	48.15, 17.15
Radiation damping times	$\tau_{x,y}$	20, 25 ms

The remainder of this paper is organized as follows. Section II describes the RW impedance model and the particle swarm optimization (PSO)-based exponential-fitting method. Section III presents the GPU-accelerated tracking algorithm. Section IV benchmarks `STABLE` by comparing its growth-rate predictions with those from `Pelegant` and theoretical formulas, using the parameters of HALF. In addition, the computational efficiency of the two tracking codes is compared. Section V uses the method to study the effects of chromaticity, bunch lengthening, filling pattern, and bunch-charge nonuniformity. Appendix A summarizes the materials and components used in the wakefield calculation for the HALF storage ring. Appendix B summarizes the theoretical growth-rate formulas, and Appendix C gives the simulation settings for `STABLE` and `Pelegant`.

II. RW WAKEFIELD AND EXPONENTIAL FITTING METHOD

A. RW wakefield

The long-range transverse RW wakefield can drive TCBI, degrading beam quality and, in severe cases, leading to beam loss. For a single-layer cylindrical vacuum chamber with infinite wall thickness, the transverse RW wakefield in the long-range approximation can be written as [14]:

$$W_{\mathrm{RW}}^{\perp}(\tau) \approx C_{\mathrm{RW}} \frac{1}{\sqrt{\tau}}, \tag{1}$$

where τ denotes the time delay of the witness particle behind the source particle, $C_{\mathrm{RW}} = \frac{L}{\pi b^3}\sqrt{\frac{Z_0 c \rho_r}{\pi}}$, L is the length of the vacuum chamber, b is the chamber radius, Z_0 is the impedance of free space, c is the speed of light, and ρ_r is the electrical resistivity of the chamber material. In practice, chamber coatings and other machine-specific factors can cause the long-range RW wakefield to deviate from Eq. (1) [31]. For this reason, the RW wakefield of a realistic storage ring is evaluated from numerically calculated impedance data.

In this work, the RW impedance model of the HALF storage ring is constructed from the impedance contributions of the relevant vacuum-chamber components listed in Table IV of Appendix A, together with their materials and resistivities. To include the distributed RW impedance in the tracking model, the transverse impedance contributions from the relevant vacuum-chamber components are represented by a single equivalent lumped impedance. The β-weighted equivalent impedance is obtained by weighting each component with its local transverse β function and summing over all components as [32]:

$$\beta_\perp Z_\perp^{\mathrm{tot}}(\omega) = \sum_j \beta_{\perp,j} Z_{\perp,j}(\omega), \tag{2}$$

where $Z_{\perp,j}(\omega)$ is the transverse RW impedance of component j, $\beta_{\perp,j}$ is the local transverse β-function value at that component, and $\beta_\perp Z_\perp^{\mathrm{tot}}(\omega)$ denotes the resulting β-weighted equivalent impedance. This construction preserves the β-weighted contribution of the distributed RW sources to the transverse wake kick and serves as input to the wakefield calculation. The corresponding β-weighted wakefield is then obtained via the inverse Fourier transform as:

$$\beta_\perp W_\perp(\tau) = \frac{i}{2\pi}\int_{-\infty}^{+\infty} e^{-i\omega\tau}\beta_\perp Z_\perp^{\mathrm{tot}}(\omega) d\omega. \tag{3}$$

The resulting wakefield is subsequently represented by a sum of exponentials for efficient tracking simulations.

B. PSO-based fitting method

Unlike the impedance-fitting approach based on a resonator model in `MuSiC`, the PSO-based wakefield fitting procedure used here directly represents the long-range transverse RW wakefield as a sum of exponentials. The fitted wakefield is written as:

$$\beta_\perp W_{\perp,\mathrm{fit}}(\tau) = \sum_{\ell=1}^{N_{\mathrm{exp}}} g_\ell \exp(-\kappa_\ell \tau), \tag{4}$$

where g_ℓ and κ_ℓ are the weight and decay rate of the ℓth exponential term, respectively. The fitting problem is then reduced to determining the coefficient set $[g_1, \kappa_1, g_2, \kappa_2, \ldots]$ over a prescribed interval $[T_0/h, N_{\mathrm{fit}} T_0]$, where T_0 is the revolution period, h is the harmonic number, and N_{fit} is the number of fitted turns. The fitting quality is evaluated using the least-squares error:

$$f_{\mathrm{obj},W} = \sum_{j=1}^{hN_{\mathrm{fit}}} [\beta_\perp W_{\perp,\mathrm{fit}}(\tau_j) - \beta_\perp W_\perp(\tau_j)]^2, \tag{5}$$

where τ_j is the jth discrete time-delay point, corresponding to the jth rf-bucket spacing behind the source particle.

Determining these coefficients is formulated as a multivariable single-objective optimization problem, with Eq. (5) as the objective function. Several optimization strategies, including PSO [33], genetic algorithm [34], and Bayesian optimization [35], were tested during method development. In the preliminary tests, PSO showed robust fitting performance over a broad parameter range and was less sensitive to the initial parameter choice. Therefore, PSO is adopted in the final implementation.

To avoid fitting errors from affecting the accuracy of growth-rate calculation, we impose an additional constraint on the reconstructed impedance at a characteristic frequency. For each exponential term, its contribution to the reconstructed impedance can be evaluated analytically as:

$$\beta_\perp Z_{\perp,\ell}(\omega) = -i\int_0^\infty g_\ell e^{-\kappa_\ell \tau} e^{i\omega\tau} d\tau = \frac{g_\ell}{\omega + i\kappa_\ell}. \tag{6}$$

Summing over all N_{exp} terms gives the impedance reconstructed from the fitted wakefield as:

$$\beta_\perp Z_{\perp,\mathrm{fit}}(\omega) = \sum_{\ell=1}^{N_{\mathrm{exp}}} \frac{g_\ell}{\omega + i\kappa_\ell}. \tag{7}$$

In the context of the present instability analysis, Eq. (B1) and the HALF vertical betatron tune ν_y indicate that the dominant vertical contribution to the growth rate is associated with the lowest-frequency betatron sideband near $0.85\ \omega_0$, where ω_0 is the angular revolution frequency. The real part of the reconstructed transverse impedance is therefore constrained at this representative frequency as:

$$|\mathrm{Re}[\beta_\perp Z_{\perp,\mathrm{fit}}(0.85\ \omega_0) - \beta_\perp Z_\perp^{\mathrm{tot}}(0.85\ \omega_0)]| \le \epsilon_Z, \tag{8}$$

where ϵ_Z is the tolerance for the impedance error. The constrained optimization problem is implemented using `pymoo` [36]. The same strategy can be extended to other key frequencies by adding the corresponding inequality constraints, although this extension is not pursued further here.

As an example, the vertical RW wakefield of HALF is fitted using a 10-term exponential expansion over the interval $[T_0/h, 200\ T_0]$. The comparison between the

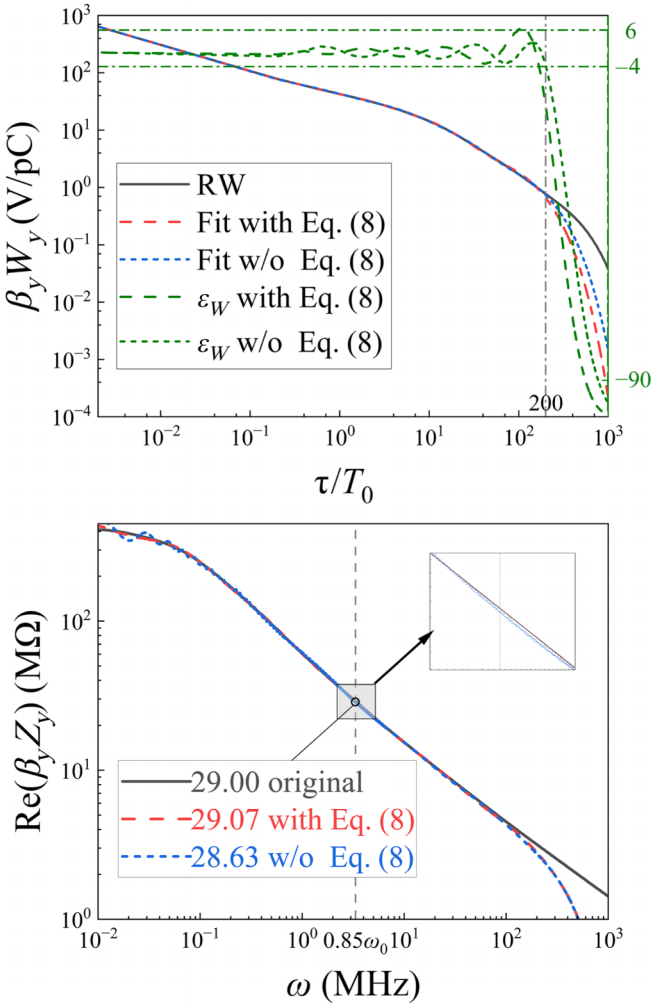


FIG. 1. Comparison between the reference long-range transverse RW wakefield and the fitted result in the time and frequency domains. The upper panel shows the vertical wakefield $\beta_y W_y$, where the green curve denotes the pointwise relative error. The lower panel shows $\mathrm{Re}(\beta_y Z_y)$ reconstructed from the fitted wakefield and compared with the original impedance. The inset gives the original and reconstructed values at 0.85 ω_0.

reference RW wakefield and the fitted result is shown in the upper panel of Fig. 1. The pointwise relative error is defined as:

$$\epsilon_W(\tau) = \frac{\beta_\perp W_{\perp,\mathrm{fit}}(\tau) - \beta_\perp W_\perp(\tau)}{\beta_\perp W_\perp(\tau)}. \tag{9}$$

Within the fitting interval, the maximum pointwise relative error is below 6%. Outside this interval, the fitted wake decays faster and eventually remains below the reference wakefield, thereby avoiding a nonphysical overestimation of the weak-wake region.

The lower panel of Fig. 1 compares the reconstructed impedance with the original impedance. The reconstructed $\mathrm{Re}(\beta_y Z_y)$ agrees well with the original impedance over the growth-rate-relevant frequency range, particularly around the lowest betatron sideband (0.85 ω_0). In particular, near 0.85 ω_0, which is closely related to the subsequent transverse-instability analysis, the relative error of the real part with the constraint of Eq. (8) is about 0.25%, compared with 1.3% without the constraint. This result indicates that the sum-of-exponentials representation preserves the relevant wakefield and impedance characteristics while enabling efficient recursive wake evaluation in multibunch tracking.

Based on Eq. (7), the same PSO framework can also be extended to frequency-domain impedance fitting, in which the exponential coefficients are determined by directly matching the reconstructed impedance to the original impedance. For example, the frequency-domain objective function can be written as:

$$f_{\mathrm{obj},Z} = \sum_{j=1}^{N_\omega} |\beta_\perp Z_{\perp,\mathrm{fit}}(\omega_j) - \beta_\perp Z_\perp^{\mathrm{tot}}(\omega_j)|^2, \tag{10}$$

where ω_j denotes the jth selected frequency sample and N_ω is the number of frequency samples. This frequency-domain extension is not pursued further in this work; instead, time-domain wakefield fitting is adopted so that the fitting interval can be directly related to the bunch-centroid memory length used in conventional multibunch tracking.

The analytical exponential construction [37] can be applied to the simplified single-layer RW wakefield described by Eq. (1). A comparison of this method with the PSO-based fitting strategy, including the number of fitting turns and the number of fitted exponential terms, has been reported in Ref. [38]. For the realistic RW wakefield considered here, which is obtained from an RW impedance model that includes effects such as chamber coatings and multilayer wall structures, the PSO-based fitting strategy remains applicable, whereas the analytical construction is mainly limited to the simplified form.

III. GPU-ACCELERATED TRACKING ALGORITHM

Efficient tracking algorithms are essential for long-term simulations, parameter scans, and instability-threshold searches in studies of collective effects. For example, observing periodic transient beam loading may require tracking over millions of turns [39], while studies of the D-mode Robinson instability often involve threshold scans over harmonic-cavity detuning [40]. These examples highlight the practical importance of improving the computational efficiency of tracking simulations.

To improve the efficiency of long-term RW tracking, the `STABLE` code has been extended with a GPU-accelerated treatment of the long-range transverse RW wakefield. The longitudinal beam dynamics follows the formulation in

Ref. [28]. The transverse RW effect is treated using an approach similar to that in Ref. [29], but omitting the complex phase-rotation component, as described below. Based on the exponential representation in Eq. (4), the wake contribution of each exponential term can be updated recursively. The voltage phasor associated with the ℓth exponential term is updated as:

$$\begin{aligned}\tilde{V}_{\ell,\mathrm{b}}(n) &= \tilde{V}_{\ell,\mathrm{a}}(n-1)e^{-\kappa_\ell T_0/h},\\ \tilde{V}_{\ell,\mathrm{a}}(n) &= \tilde{V}_{\ell,\mathrm{b}}(n) + \tilde{V}_{\ell,0}(n),\\ \tilde{V}_{\ell,0}(n) &= q_n g_\ell F_\ell(n).\end{aligned} \tag{11}$$

Here n denotes the rf-bucket index in the recursive update. At each bucket step, the voltage phasor is first propagated over one bucket spacing T_0/h. The quantities $\tilde{V}_{\ell,\mathrm{b}}(n)$ and $\tilde{V}_{\ell,\mathrm{a}}(n)$ are the voltage phasors before and after the passage of the nth bucket, respectively. The term $\tilde{V}_{\ell,0}(n)$ is the new voltage phasor excited by the bunch charge q_n in bucket n; for an empty bucket, $q_n = 0$, and therefore $\tilde{V}_{\ell,0}(n) = 0$. The form factor $F_\ell(n)$ describes the contribution of the longitudinal distribution and transverse offset of the source bunch to the excited voltage phasor. In the following, the vertical plane is used as an example, while the horizontal plane can be treated similarly. For a bunch with normalized longitudinal density $\rho_n(\tau)$ obtained directly from the tracked macroparticle distribution, $F_\ell(n)$ is defined as:

$$F_\ell(n) = \int_{-\infty}^{\infty} \rho_n(\tau) y_n(\tau) e^{\kappa_\ell \tau}\, d\tau, \tag{12}$$

where $y_n(\tau)$ is the transverse offset at longitudinal position τ. In macroparticle tracking, this quantity can be evaluated directly without slicing the bunch. For equal-weight macroparticles, it is given by:

$$F_\ell(n) = \frac{1}{N_p}\sum_{j=1}^{N_p} y_{n,j}\, e^{\kappa_\ell \tau_{n,j}}, \tag{13}$$

where N_p is the number of macroparticles in the bunch and $y_{n,j}$ and $\tau_{n,j}$ are the transverse position and the longitudinal coordinate of the jth macroparticle relative to the reference position of bucket n, respectively. This particle-based form avoids explicit longitudinal slicing and is suitable for GPU-parallel computation. It also retains the longitudinal dependence of the source bunch, which is lost in a point-bunch representation.

In the long-range RW treatment considered here, the field induced by the passage of a bunch is not applied back to the same bunch; only wake interactions between different bunch passages are included. The effective transverse voltage experienced by the jth macroparticle in bunch n is obtained by summing the contributions from all fitted exponential terms as:

$$V_j(n) = \sum_{\ell=1}^{N_{\mathrm{exp}}} \tilde{V}_{\ell,\mathrm{b}}(n) e^{-\kappa_\ell \tau_{n,j}}. \tag{14}$$

The corresponding transverse kick is given by:

$$\Delta y'_j(n) = \frac{eV_j(n)}{E_0}. \tag{15}$$

This recursive formulation replaces the explicit convolution over the bunch-centroid history with bucket-by-bucket phasor updates for the fitted exponential terms, thereby reducing both memory usage and computational cost. In this implementation, the phasors are updated sequentially over the h rf buckets within each turn because each bucket depends on the preceding one. However, the computational work associated with this sequential update is small compared with particle-level tracking operations, and therefore it does not become a computational bottleneck.

For betatron oscillations, the transverse linear one-turn map, as well as synchrotron-radiation damping and quantum excitation, follow the formulation of the `STABLE` code described in Ref. [29]. We therefore refer the reader to Ref. [29] for the implementation details of the transverse map, radiation damping, and quantum excitation. In the following simulations, TCBI results are presented for the vertical plane, which gives higher growth rates than the horizontal plane for the HALF parameters. Transverse coupling is not included. The vertical emittance is set to $\epsilon_y = 1$ pm rad, since it is usually much smaller than the horizontal emittance.

IV. BENCHMARK AND EFFICIENCY TEST

A. Benchmark test

To verify the reliability of the newly developed treatment of the long-range transverse RW wakefield in `STABLE`, the growth rates for the uniform-filling pattern are compared among three predictions: `STABLE` code with the new recursive RW treatment, the well-established `Pelegant` code [20,21], and the theoretical prediction from Eq. (B2) in Appendix B, which takes as input the rms length of the bunch. The detailed settings of the two tracking programs are given in Appendix C.

As shown in Fig. 2, we first analyze the convergence of `Pelegant` simulations with respect to the number of retained turns using the original wakefield, and the results are compared with the theoretical growth rates computed from the original impedance. The convergence is achieved after 160 retained turns. The growth rates are then computed using `STABLE` with the fitted wakefield data and compared with the theoretical values calculated from the impedance reconstructed from the fitted wakefield,

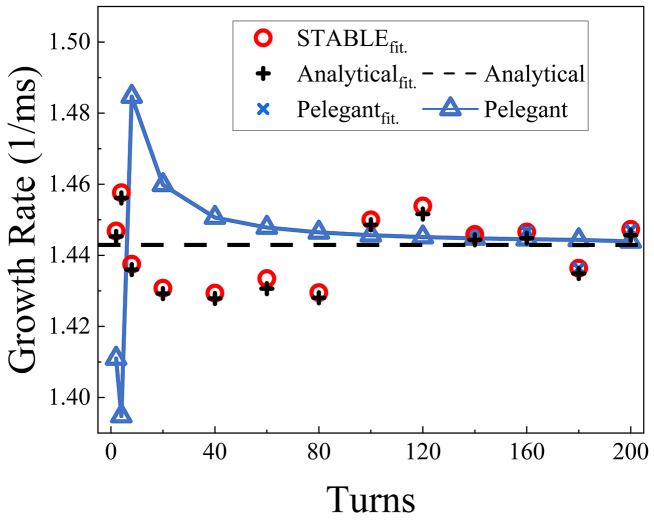


FIG. 2. Growth rate comparison: Lines are obtained from the original wakefield or impedance (black: theory, blue: `Pelegant`); markers are obtained from the fitted wakefield with 10 exponential terms or from the reconstructed impedance (red circles: `STABLE`, blue crosses: `Pelegant`, black crosses: theory).

showing good agreement. Finally, the growth rates obtained from `Pelegant` using the fitted wakefield (only converged results are shown) are compared with those from `STABLE` and the theory. `Pelegant` with the fitted wakefield also shows excellent agreement with both `STABLE` and the theoretical reference after convergence. This verifies the correctness of the fitting method. Although minor fluctuations are observed as the fitting length varies, the result obtained using the 200-turn fitted wakefield remains in good agreement with the original-impedance reference. Therefore, unless otherwise stated, the 200-turn fitted wakefield with 10 fitted exponential terms is adopted in all subsequent `STABLE` simulations, as it provides sufficient accuracy for the benchmark and application studies considered here.

Bunch lengthening and positive chromaticity are effective measures for suppressing transverse RW instabilities in diffraction-limited storage rings [41]. For HALF, bunch lengthening is planned to be achieved using a superconducting passive third-harmonic cavity with $R/Q = 40.5\ \Omega$ and a quality factor $Q = 2 \times 10^8$. The equilibrium bunch length is controlled by the harmonic-cavity detuning Δf_r, which changes the longitudinal equilibrium potential well. Figure 3(a) shows the TCBI growth rate as a function of ξ_y for three representative bunch lengths obtained with a passive harmonic cavity under uniform filling, corresponding to $\Delta f_r = 300$ kHz with negligible lengthening, 60 kHz with approximately 3 times the natural bunch length, and 50 kHz with overlengthening. Their corresponding bunch profiles are shown in Fig. 3(b). In the following simulations, the harmonic cavity is included to model the bunch-lengthening effect. Increasing positive chromaticity and lengthening the bunch both reduce the

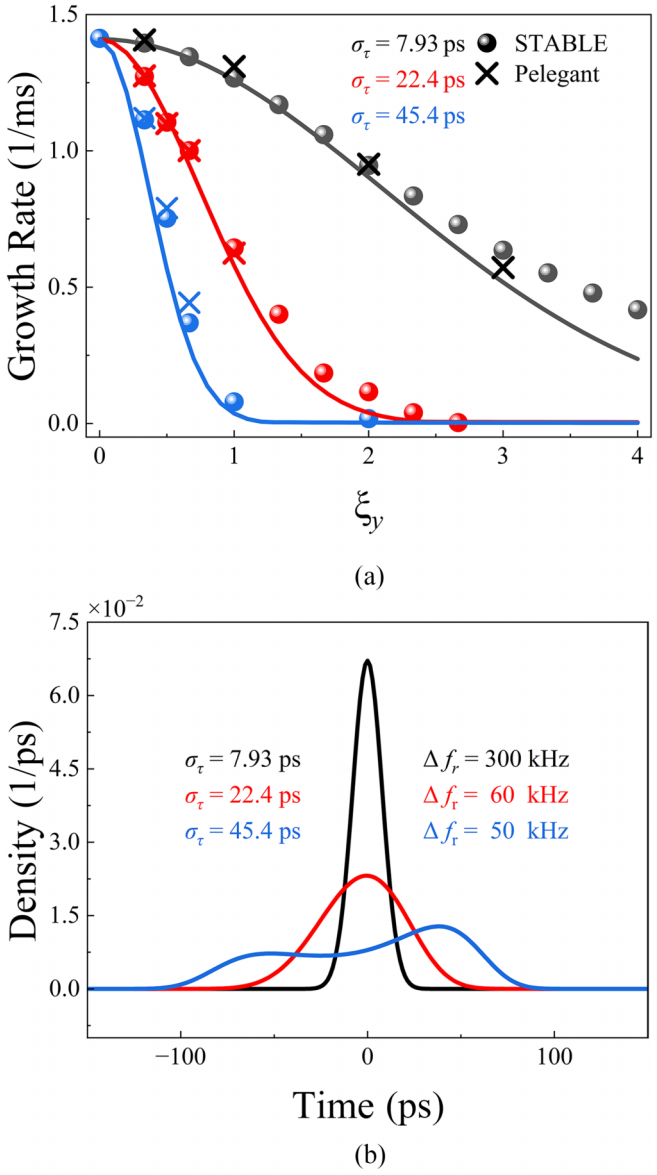


FIG. 3. (a) Growth rate as a function of ξ_y for three bunch lengths σ_τ. Lines: theory; markers: `STABLE` (red circles) and `Pelegant` (blue crosses). (b) Bunch profiles for the same three cases: $\Delta f_r = 300$ kHz (negligible lengthening), 60 kHz (3 times natural length), and 50 kHz (overlengthened).

transverse RW instability growth rate, and the theoretical predictions agree well overall with the tracking results from both `STABLE` and `Pelegant`. However, at relatively large chromaticities, small discrepancies between the tracking results and theoretical predictions can be observed, mainly because the theoretical derivation relies on the small-chromaticity approximation.

B. Efficiency test

The two tracking codes ran on distinct platforms: `STABLE` on a personal computer (PC) with an Intel Core Ultra 7 265K CPU and an NVIDIA RTX 5070

TABLE II. Computational time (min $/(10^4$turns)) for STABLE and Pelegant versus the parameter N, where $N = N_{\mathrm{fit}}$ (fitting length) for STABLE and $N = N_{\mathrm{ret}}$ (retained centroid-history length) for Pelegant.

N	STABLE	Pelegant w/o WATCH	Pelegant w/ WATCH	Pelegant w/ WATCH + RFMODE
20	1.67	137	305	377
40	1.66	252	441	473
100	1.67	612	774	804
200	1.68	1145	1350	1402

GPU (6144 CUDA cores), the CPU and GPU together costing about $900; and Pelegant on a server using 90 AMD EPYC 9654 CPU cores, the CPU alone costing about $10 000, excluding other server components. The estimated cost of the main computing components for the server is therefore roughly 1 order of magnitude higher than that for the PC. Table II compares the computational time required for every 10^4 turns under different values of the fitting length N_{fit} for STABLE and the retained centroid-history length N_{ret} for Pelegant. The STABLE run-time includes bunch lengthening and bunch-centroid export for growth-rate analysis, while the Pelegant results are shown for three configurations with different combinations of WATCH output and RFMODE. Because the recursive formulation in STABLE does not store or convolve the bunch-centroid history, its computational cost is nearly independent of the fitting length N_{fit} used to construct the fitted wakefield. By contrast, Pelegant uses history-based convolution, whose cost increases with the retained bunch-centroid history length N_{ret}. As a result, the run-time of STABLE remains nearly constant at about 1.67 min $/10^4$ turns for all tested N_{fit}, whereas the run-time of Pelegant increases significantly with N_{ret}. The additional WATCH output and RFMODE element further increase the computational cost.

It should be noted that the present STABLE simulation uses 4D tracking in (z, δ, y, y'), while Pelegant performs 6D tracking in $(z, \delta, y, y', x, x')$. As a conservative estimate, even if extending STABLE from 4D to 6D tracking approximately doubled the run-time, STABLE would remain about 2 orders of magnitude faster than Pelegant under the tested configurations. Overall, these results demonstrate that the exponential-fitting-based treatment implemented in STABLE provides substantially higher computational efficiency than the conventional convolution method while maintaining high accuracy and low hardware cost.

V. APPLICATIONS

A. Uniform filling

The benchmark results in Sec. IV verify the accuracy of the present tracking method for representative cases. For practical operation, however, these discrete cases are not sufficient to identify the stable parameter region nor to select a practical working point. Therefore, we further perform a two-dimensional scan over the harmonic-cavity detuning Δf_r and the vertical chromaticity ξ_y under uniform filling. For each detuning, the longitudinal equilibrium distribution is calculated using the semianalytical method in Ref. [42], and the corresponding rms bunch length is extracted. The resulting relation between Δf_r and the equilibrium rms bunch length is shown in Fig. 4. In the following scans, the harmonic-cavity detuning Δf_r is used as the actual scan variable, and varying Δf_r allows us to obtain different equilibrium bunch lengths. The relation between the bunch length σ_τ and Δf_r is approximately given by an empirical formula as:

$$\sigma_\tau = \frac{5.97\Delta f_r + 32.39}{\Delta f_r - 42.78}, \tag{16}$$

where σ_τ denotes the rms bunch length corresponding to a given detuning Δf_r. Here Δf_r is expressed in kHz and σ_τ in ps. This conversion is used only to relate the detuning scan more directly to bunch lengthening in the figures and is not used in the tracking calculation or physical modeling. Using Δf_r as the scan variable is also convenient for the later nonuniform filling analysis, where the equilibrium bunch length may vary from bunch to bunch.

Figure 5 shows the growth rates obtained from a two-dimensional STABLE scan over Δf_r and ξ_y. We choose a

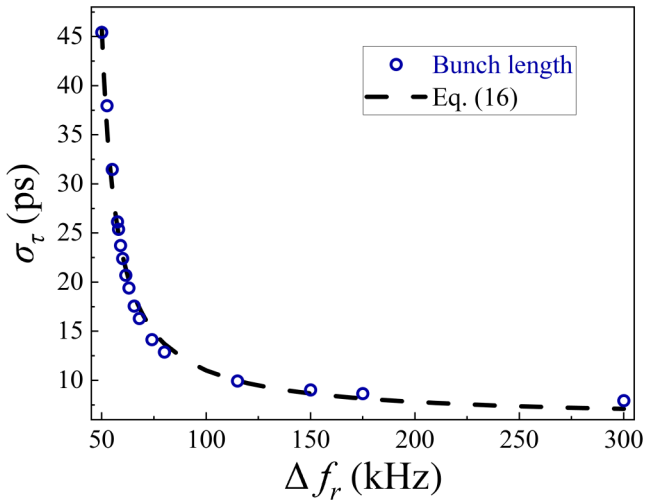


FIG. 4. Relation between the detuning Δf_r of the superconducting third-harmonic cavity and the equilibrium rms bunch length.

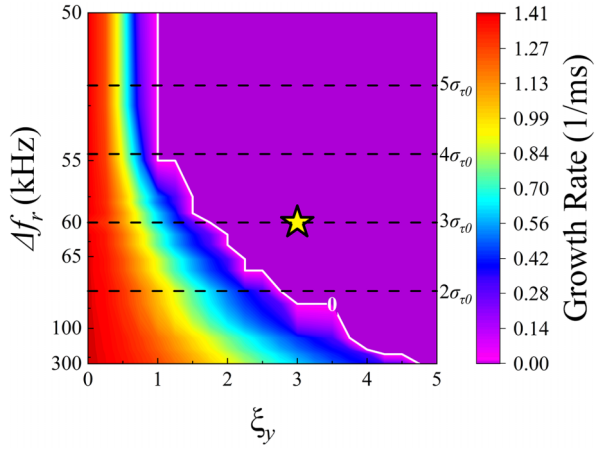


FIG. 5. Two-dimensional scan of the transverse RW instability growth rate as a function of Δf_r and ξ_y. The white solid line separates the stable and unstable regions, the black dashed lines indicate selected rms bunch lengths corresponding to the detuning axis, and the yellow star denotes the baseline working point.

conservative bunch length of $\sigma_\tau = 22.4$ ps, corresponding to $\Delta f_r = 60$ kHz, as the baseline, although a longer bunch would further suppress the transverse RW instability. This working point is marked by the yellow star in the figure. At this point, the maximum growth rate is lower than the transverse radiation damping rate, indicating that the beam is stable with a certain margin from the stability boundary. These results confirm that the baseline provides sufficient stability margin for the HALF operation. The full two-dimensional scan takes about one day with `STABLE`, whereas the same point-by-point scan using `Pelegant` with $N_{\mathrm{ret}} = 200$ is estimated to require about 2 years, based on the results in Table II.

B. Nonuniform filling

In high-current electron storage rings, nonuniform filling patterns with a fraction of empty buckets are commonly adopted to mitigate ion instabilities [43]. Many third-generation light sources have operated with a long multibunch train and a dedicated ion-clearing gap. In hybrid filling modes, one or several isolated bunches may also be placed in the gap to provide timing pulses [44,45]. For fourth-generation storage-ring light sources, harmonic cavities are frequently used to lengthen the bunches, thereby improving beam quality and stability. However, a single long train is not favorable for harmonic-cavity-induced bunch lengthening. Multiple identical subtrains, with empty buckets distributed more uniformly around the ring, are therefore often preferred [46–50] to satisfy both bunch lengthening and ion-instability suppression. For the HALF storage ring, we consider filling patterns in which the buckets are divided into 20, 10, or 5 identical subtrains, with total filling fractions of 70%, 80%, and 90%. A conventional long-train filling pattern is also included as a reference. To compare different filling fractions on an equal-current basis, the total beam current is kept fixed at 350 mA. A schematic illustration of these filling patterns is shown in Fig. 6. To benchmark the treatment of nonuniform filling patterns, Table III compares the growth rates predicted by Eq. (B6), which assumes a fixed bunch length of 7.93 ps, with those extracted from `STABLE` tracking for the short-bunch case with $\Delta f_r = 300$ kHz and $\xi_y = 0$. The relative errors remain below 2% for all tested filling patterns and filling fractions, showing that the `STABLE` tracking results are consistent with the theoretical benchmark given by Eq. (B6) for nonuniform filling patterns.

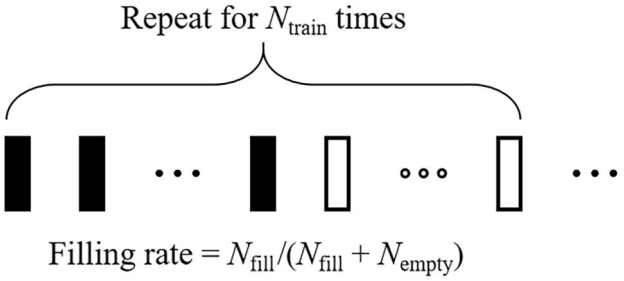


FIG. 6. Schematic illustration of the nonuniform filling.

A full scan over the considered filling patterns is then carried out, with chromaticity scanned from 0 to 5 in steps of 0.5 and 9 detuning frequencies selected in the range of 50–300 kHz; using Eq. (16), the corresponding bunch lengths (computed for the uniform-filling case) are approximately uniformly distributed from 7.93 to 45.4 ps. As shown in Fig. 7, the long-train filling pattern generally gives larger growth rates than the multitrain cases. For the long-train cases, at $\Delta f_r = 60$ kHz and $\xi_y = 3$, the 70% and 80% filling fractions remain unstable, while the 90% filling fraction satisfies the stability criterion but with a relatively small stability margin. In contrast, the other nine multitrain cases are stable at this working point and show clearer stability margins. In the lower-right part of Fig. 7, a reduced stable region is observed under the overlengthened condition, roughly bounded by the 70%—20-train, 80%—10-train, and 90%—5-train cases. The overlengthened condition at $\Delta f_r = 50$ kHz increases the growth rate and causes this reduction; for example, a point that is stable at $\Delta f_r = 55$ kHz and $\xi_y = 1.5$ may become unstable when the detuning is decreased to $\Delta f_r = 50$ kHz.

One important reason for the difference observed in Fig. 7 is the bunch-by-bunch variation of the equilibrium σ_τ caused by transient beam loading in the harmonic cavity under nonuniform filling, as shown in Fig. 8. For the long-train filling patterns, the bunch-lengthening effect is significantly weaker than that in the multitrain cases, which explains why the stable region in the first column of Fig. 7 differs noticeably from those in the other

TABLE III. Comparison of growth rates obtained from the theory of Bassi *et al.* [17] and `STABLE` tracking.

Filling pattern	Filling rate	Formula (1/ms)	Tracking (1/ms)	Relative error
Long train	70%	1.525	1.527	0.13%
	80%	1.467	1.473	0.41%
	90%	1.425	1.451	1.82%
5 trains	70%	1.434	1.462	1.95%
	80%	1.419	1.432	0.92%
	90%	1.409	1.415	0.43%
10 trains	70%	1.419	1.434	1.06%
	80%	1.412	1.435	1.63%
	90%	1.407	1.431	1.71%
20 trains	70%	1.412	1.429	1.20%
	80%	1.408	1.413	0.36%
	90%	1.406	1.410	0.28%

columns. For the other nine multitrain cases, the filling pattern has a relatively small influence on the average bunch length for detunings below about 60 kHz. At 50 kHz, although the bunch-by-bunch variation is still visible, the average bunch length is sufficiently large that the instability can be suppressed once ξ_y is increased to about $\xi_y = 3$.

Nonuniform filling does not reduce the RW-driven TCBI growth rate in all cases considered here but instead leads to a slight enhancement. To clarify this behavior, we use the model proposed by Bassi *et al.* [17] see Eq. (B4) in Appendix B to reveal the role of the filling pattern, although the original model assumes zero chromaticity while our tracking includes chromaticity and bunch-length

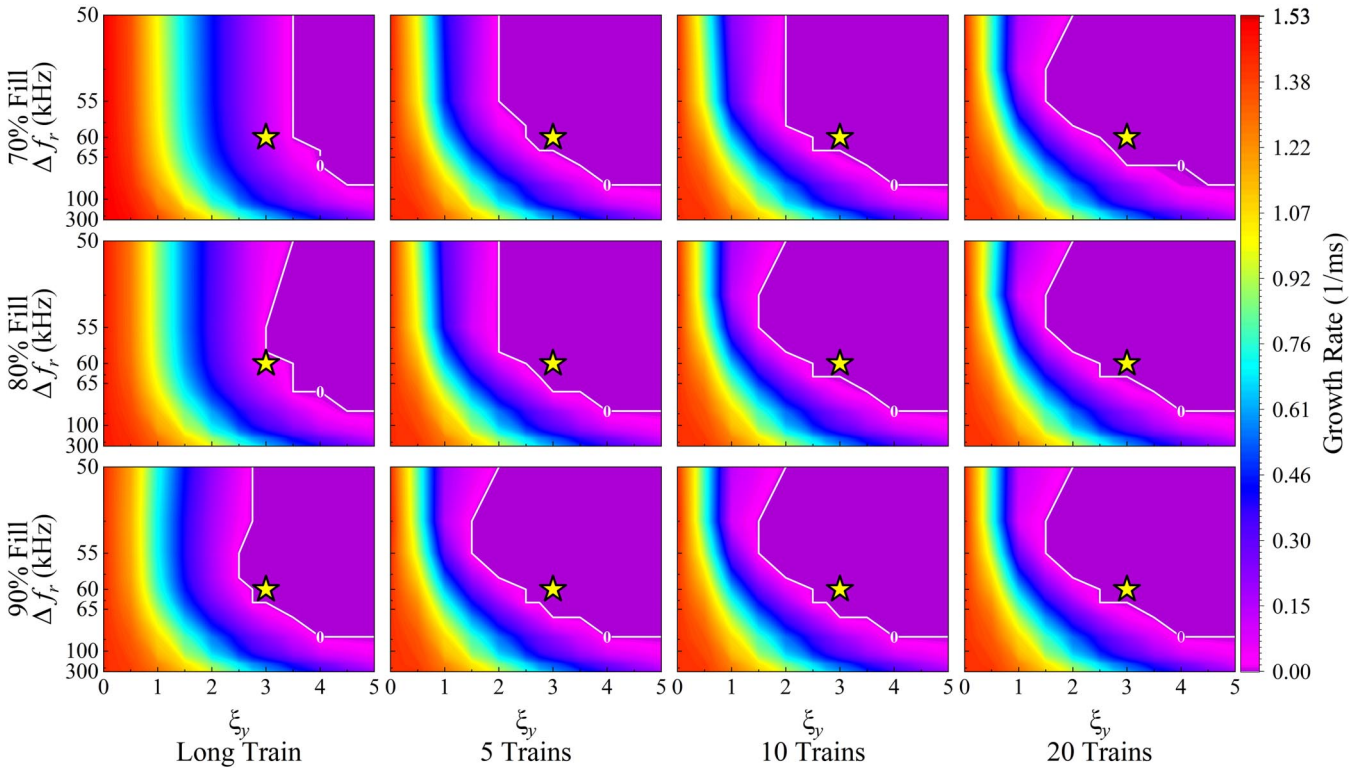


FIG. 7. Two-dimensional scan results of coupled-bunch instability growth rates with respect to Δf_r and ξ_y under nonuniform filling patterns. Rows correspond to 70%, 80%, and 90% filling fractions; columns correspond to the long-train, 5-train, 10-train, and 20-train patterns. The white solid lines separate the stable and unstable regions, and the yellow stars denote the baseline working points. The y axis is transformed using Eq. (16).

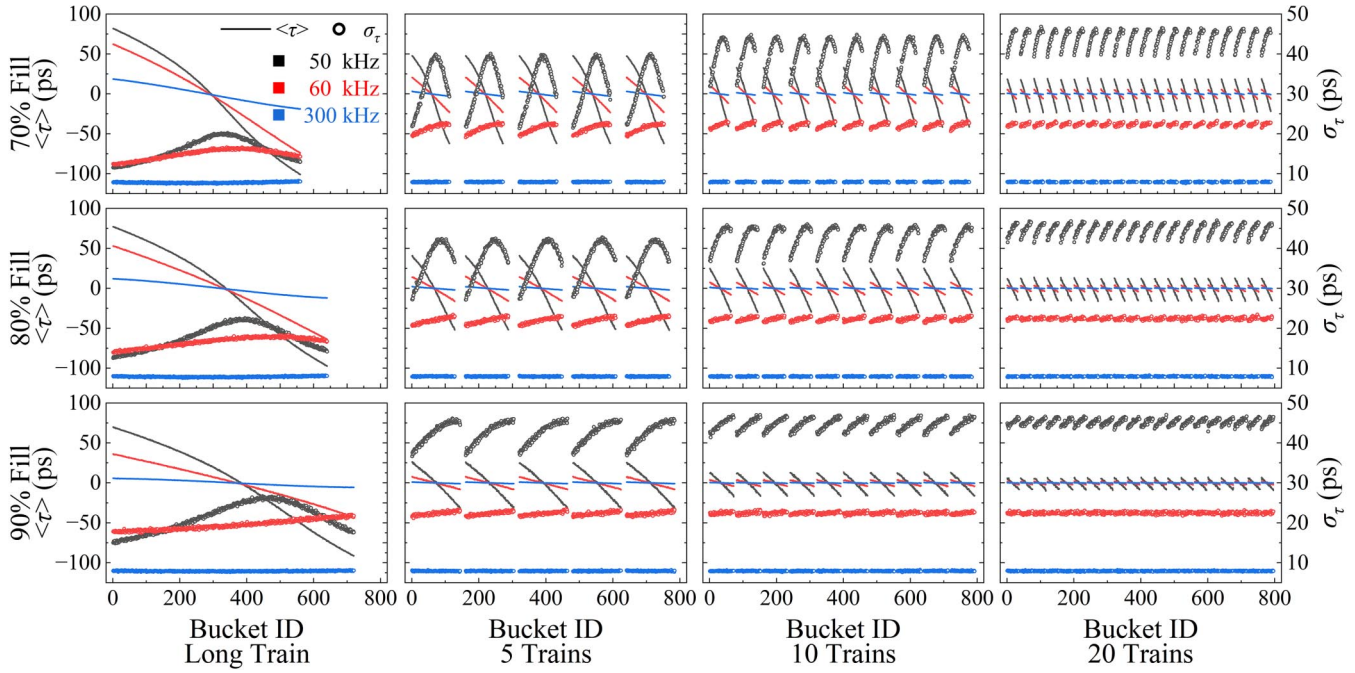


FIG. 8. Bucket-by-bucket distributions of centroid $\langle\tau\rangle$ and bunch length σ_τ for various nonuniform filling patterns and harmonic-cavity detunings Δf_r. Rows correspond to 70%, 80%, and 90% filling fractions; columns correspond to long-train, 5-train, 10-train, and 20-train patterns. Black, red, and blue correspond to $\Delta f_r = 50$, 60, and 300 kHz, respectively; for each detuning, markers represent σ_τ, and solid lines represent $\langle\tau\rangle$.

variation. The RW impedance can drive many unstable coupled-bunch modes. As a result, the filling-pattern-induced mode mixing involves a wide range of unstable modes and stable modes. This behavior differs from the fill-pattern stabilization discussed in Ref. [51], where the instability is mainly dominated by a small number of coupled-bunch modes. In the present case, the fill-pattern modulation leads to broad mode mixing, and the resulting largest eigenvalue of **B** increases slightly, giving a larger maximum growth rate than that in the uniform-filling case.

Combining 12 filling patterns, 11 chromaticity values, and 9 detuning frequencies yields a total of 1188 cases. To accelerate this scan, we exploit two strategies. First, because the equilibrium distribution is nearly independent of chromaticity for a given filling pattern and detuning, we compute it only once for each pattern-detuning combination and reuse it across all chromaticities, avoiding a separate 40 000-turn equilibration for every case. Second, we adopt an early-termination criterion: the simulation stops as soon as the centroid amplitude grows sufficiently to clearly identify the unstable mode and reliably estimate its growth rate; in practice, this usually requires only a few thousand turns instead of the full 10 000. Together, these measures ensured that the complete 1188-case scan with STABLE was finished within 2 days.

C. Nonuniform bunch charge

In actual storage-ring operation, the charges of different bunches usually have certain variations. To evaluate the influence of bunch-to-bunch charge nonuniformity on TCBI, numerical simulations are performed for different filling patterns at a fixed filling fraction of 90%. In the simulation, the charge of the jth bunch is written as:

$$q_j = q_0 C_{\text{charge},j}, \tag{17}$$

where q_0 is the single-bunch charge in the uniform-charge case, and $C_{\text{charge},j}$ is a random charge factor. A truncated Gaussian distribution is used to generate $C_{\text{charge},j}$, with a mean value of 1 and a standard deviation of σ_{charge}, while ensuring that all bunch-charge factors remain positive. To exclude the effect of changes in the total beam current on the instability growth rate, the random charge factors are further normalized as:

$$C_{\text{charge},j} \leftarrow \frac{C_{\text{charge},j}}{\langle C_{\text{charge}}\rangle}, \tag{18}$$

so that the total beam current is kept constant for different random charge distributions.

The charge-nonuniformity scan is performed for three representative operating conditions, with the detuning fixed at 60 kHz and ξ_y set to 0, 1, and 2. For each value of σ_{charge}, nine independent random charge distributions are generated, and the growth rate is recorded for each seed. The results are shown in Fig. 9, where the markers represent the average growth rates over the nine seeds and

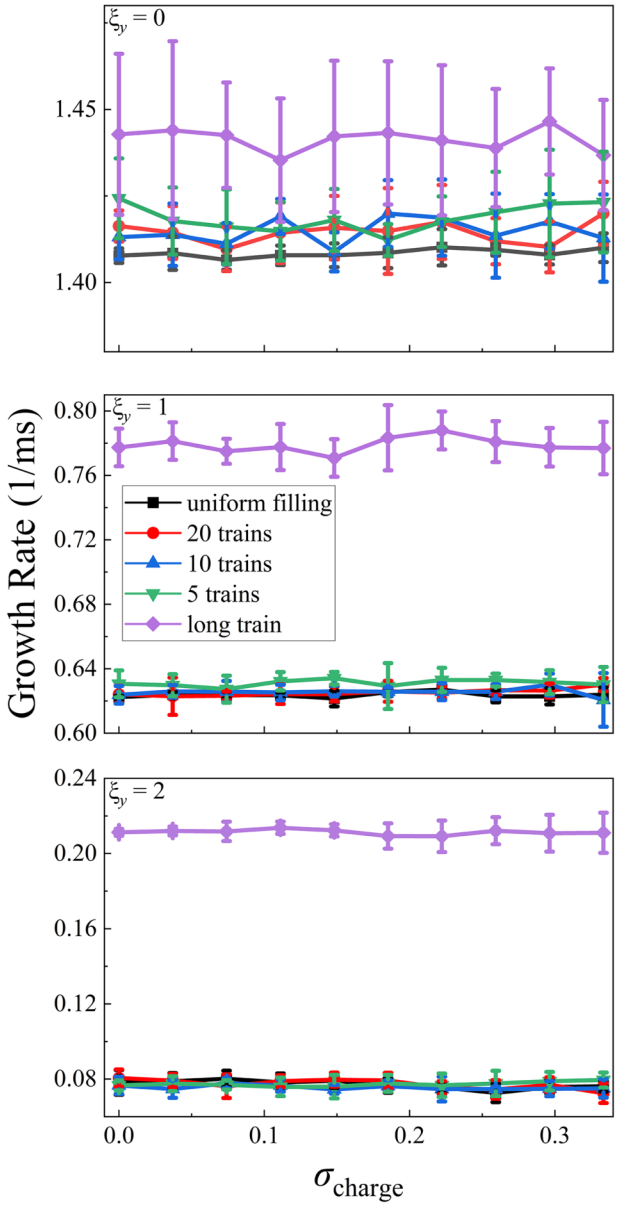


FIG. 9. Coupled-bunch instability growth rate as a function of σ_{charge} for different filling patterns at $\Delta f_r = 60$ kHz. The three panels correspond to $\xi_y = 0, 1,$ and 2, respectively. Different colors represent different filling patterns, and the error bars denote the standard deviations over nine independent random seeds.

the error bars denote the corresponding standard deviations. Within the scanned range of σ_{charge}, both the mean growth rate and the seed-to-seed fluctuation vary only moderately, and no clear monotonic dependence on σ_{charge} is observed. Compared with bunch-charge nonuniformity, chromaticity and filling pattern have much more pronounced effects on the mean growth rate. For all three chromaticities, the long-train filling pattern gives the largest average growth rate among the considered filling patterns. At $\xi_y = 0$, the nonuniform filling patterns generally give larger growth rates than the uniform-filling case, whereas at $\xi_y = 1$ and $\xi_y = 2$, except for the long-train pattern, the growth rates of the 20-train, 10-train, and 5-train patterns are close to the uniform-filling result. These results indicate that bunch-charge nonuniformity mainly introduces seed-dependent fluctuations in the growth rate, while the average growth-rate level is still primarily determined by the filling pattern and chromaticity.

VI. SUMMARY AND OUTLOOK

The exponential-fitting method for efficient treatment of the long-range transverse RW wakefield has been developed and implemented in the GPU-accelerated code `STABLE`. The RW wake is represented as a sum of exponentials with coefficients determined by the PSO algorithm, converting the conventional history-dependent convolution into a recursive update that eliminates the need to store the bunch-centroid history. This fitted wake accurately reproduces the reference wake and preserves the relevant impedance characteristics at the dominant instability frequency. Benchmark simulations with HALF parameters show good agreement with theoretical predictions and `Pelegant` tracking. Efficiency tests show that `STABLE` achieves over 2 orders of magnitude speedup over the convolution-based tracking in `Pelegant`, while at roughly one-tenth of the hardware cost. The method was subsequently applied to large-scale parameter scans with HALF parameters, covering the effects of chromaticity, bunch lengthening, nonuniform filling patterns, and bunch-charge nonuniformity on the RW-driven TCBI. These applications demonstrate the capability of the method for efficient multiparameter instability analysis in high-current storage rings.

The reduction in computation time by orders of magnitude enables long-range RW tracking to be incorporated into automated optimization loops. Future work will integrate the fast tracking engine with optimization algorithms [52] or artificial intelligence agents [53] to automate simulation, stability evaluation, and the exploration of optimal operating conditions, advancing toward more intelligent and efficient beam dynamics studies.

ACKNOWLEDGMENTS

This work was supported by the National Natural Science Foundation of China (No. 12375324, No. 12105284, and No. 12475158) and the Fundamental Research Funds for the Central Universities (No. WK2310000127).

DATA AVAILABILITY

There are no publicly available research data or software supporting this manuscript. Requests for further information or data should be sent to the authors.

APPENDIX A: RW IMPEDANCE CALCULATION

The vacuum-chamber components used in this work are summarized in Table IV, which details the component dimensions, materials, and the corresponding beta functions used in the wakefield calculation. The resistivity of the nonevaporable getter (NEG) coating is 1×10^{-6} Ω m, while the other materials are assigned their common resistivities. The RW impedance data were calculated using the `IW2D` code [54]. For the elliptical chamber, the circular-chamber result was first calculated using a radius equal to the semiminor axis of the ellipse and then corrected using Yokoya factors [55].

APPENDIX B: THEORY OF TCBI

In the limit of the point-bunch approximation and zero chromaticity, and retaining only the dominant term corresponding to the impedance sampled at the smallest absolute frequency, the growth rate τ_μ^{-1} of the transverse coupled-bunch instability driven by the RW impedance can be calculated as [14]:

$$\tau_\mu^{-1} = \frac{I_0 c}{2E_0 C}\,\mathrm{Re}[\beta_\perp Z_\perp(-(\mu+\nu)\omega_0)], \tag{B1}$$

where $\nu = \omega_\beta/\omega_0$ is the betatron tune and ω_β is the transverse betatron angular frequency.

However, under realistic operating conditions, the bunch length is finite, and the chromaticity may be nonzero, which limits the applicability of the simplified formula. Therefore, an expression based on Sacherer's theory [15] can be used to include the effects of finite bunch length and nonzero chromaticity ξ. Here, the simplified form given by Bassi *et al*. [56] is adopted as:

$$\tau_\mu^{-1} = -\frac{I_0}{2T_0E_0}\sum_{p=-\infty}^{+\infty}|\tilde{\lambda}(\omega_{p\mu}-\omega_\xi)|^2\mathrm{Re}[\beta_\perp Z_\perp(\omega_{p\mu})], \tag{B2}$$

where I_0 is the average total beam current and E_0 is the beam energy in eV. $\omega_{p\mu} = ph\omega_0 + \mu\omega_0 + \omega_\beta$. The chromatic frequency shift is $\omega_\xi = \omega_0\xi/\eta$, with $\eta = \alpha_c - 1/\gamma^2$ being the slippage factor, and α_c and γ are the momentum compaction factor and the relativistic Lorentz factor, respectively. For a Gaussian longitudinal distribution, the bunch spectrum is $\tilde{\lambda}(\omega) = \exp[-(\omega\sigma_\tau)^2/2]$.

For arbitrary nonuniform filling patterns or nonuniform bunch-charge distributions at zero chromaticity, the more general formula extended by Bassi *et al*. [17] can be used. In this method, the coupled matrix B is constructed to solve for the eigenmode growth rates of the multibunch system in the storage ring. The relevant expressions are

$$\Omega_\mu = -\frac{iI_0}{2T_0E_0}\sum_{p=-\infty}^{+\infty}|\tilde{\lambda}(\omega_{p\mu})|^2\beta_\perp Z_\perp(\omega_{p\mu}) \tag{B3}$$

and

$$\mathbf{B} = \mathbf{\Omega M}, \quad \mathbf{\Omega} = \mathrm{diag}(\Omega_0, \Omega_1, \ldots, \Omega_{h-1}),$$
$$M_{\mu\mu'} = \frac{1}{N_T}\sum_{m=0}^{h-1} N_m e^{i2\pi m(\mu'-\mu)/h}, \tag{B4}$$

where $\mu, \mu' = 0, 1, \ldots, h$–1 and N_m is the bunch charge in the mth rf bucket; for an empty bucket, $N_m = 0$. For uniform filling, $\mathbf{M}$ reduces to the identity matrix, and all coupled-bunch modes remain independent. For nonuniform filling, the off-diagonal elements of $\mathbf{M}$ couple different modes, so that the eigenmodes become linear combinations of the original coupled-bunch modes. The total bunch charge is

TABLE IV. Parameters for the HALF resistive-wall wakefield calculation. Apertures are given as diameter (circular) or major × minor axis (elliptical).

Element no.	Layers	Material (thickness) per layer (inner to outer)	Aperture (mm)	Length (m)	β_x (m)	β_y (m)
1	2	NEG (1 μm) + CuZr (1 mm)	∅26	241.08	4.56	6.22
2	2	NEG (1 μm) + 316LN (5 mm)	∅26	15.53	2.67	8.20
3	2	NEG (1 μm) + Inconel (0.5 mm)	∅26	5.60	4.54	4.91
4	2	NEG (1 μm) + CuCrZr (1 mm)	∅26	12.78	4.10	6.99
5	1	316LN (5 mm)	∅26	2.39	4.32	6.59
6	1	CuZr (1 mm)	∅26	20.13	6.42	5.08
7	1	CuCrZr (1 mm)	∅26	6.31	1.03	15.62
8	2	Cu (20 μm) + 316LN (1 mm)	∅26	87.91	0.75	5.89
9	2	Ag (7.5 μm) + 316LN (5 mm)	∅26	26.40	4.19	6.72
10	1	Al (1 mm)	26 (H) × 12.6 (V)	4.56	7.02	3.20
11	1	Al (1 mm)	26 (H) × 9.0 (V)	4.56	7.02	3.20
12	1	Al (1 mm)	26 (H) × 8.0 (V)	35.84	7.02	3.20
13	3	Cu (75 μm) + Ni (75 μm) + NdFeB (3 mm)	65 (H) × 5.7 (V)	5.40	6.02	2.93

$$N_T = \sum_{m=0}^{h-1} N_m. \tag{B5}$$

By solving the eigenvalue problem of the matrix B, the eigenvalues Ω'_j are obtained from:

$$|\mathbf{B} - \Omega'_j \mathbf{I}| = 0. \tag{B6}$$

The eigenmode growth rates under nonuniform filling are then given by $\mathrm{Im}(\Omega'_j)$, with the maximum growth rate determined by the largest imaginary part.

APPENDIX C: STABLE AND PELEGANT SIMULATION SETTINGS

In the tracking simulations reported in this work, both `STABLE` and `Pelegant` use 5000 macroparticles per bunch as a compromise between computational cost and statistical noise. For the HALF parameters under uniform filling, this choice was verified to be converged: the growth rates obtained with 5000, 10 000, and 50 000 macroparticles per bunch are 1.4472, 1.4474, and 1.4473 ms^{-1}, respectively, differing by less than 0.02%, so 5000 macroparticles per bunch are sufficient. In all simulations reported in this work, `STABLE` uses 4D tracking in (z, δ, y, y'), whereas `Pelegant` is a 6D tracking code that tracks in $(z, \delta, y, y', x, x')$. The longitudinal short-range wakefields of the rf cavities are omitted because they have a negligible effect on bunch lengthening for the HALF parameters considered in this work [57].

`STABLE` includes the following longitudinal effects: the main rf cavity, the passive third-harmonic cavity, transient beam loading, and synchrotron-radiation damping with quantum excitation. The details of the implementation can be found in Ref. [28]. The transverse effects are those described in Sec. III. In each simulation, the bunches are first tracked for a number of turns to reach longitudinal equilibrium, since the initial longitudinal Gaussian distribution may not match the phase-space distribution; if the beam is not equilibrated, the varying bunch length would degrade the accuracy of the subsequent growth-rate extraction. During this stage, all the longitudinal effects listed above are active, whereas only radiation damping, quantum excitation, and betatron oscillations are included in the transverse plane. After equilibrium is reached, a transverse displacement of about 1 μm is applied to the head bunch as the initial perturbation and the long-range transverse RW wakefield is turned on; the resulting longitudinal distribution is not frozen but continues to evolve together with the transverse-instability tracking under the action of the longitudinal effects.

In `Pelegant` release 2023.4, which is based on the MPI distribution MPICH 4.0, the `ILMATRIX` element is used to generate the linear transfer matrix for the particles, with transverse coupling between the horizontal and vertical planes disabled. Synchrotron-radiation damping and quantum excitation are enabled using the `SR` element. The radiation damping partition numbers are set to $J_x = 0.926$, $J_y = 0.741$, and $J_\delta = 1.324$, corresponding to damping times of 20, 25, and 14 ms, respectively. A main rf cavity is used to maintain the energy of the synchronous particle. When harmonic-cavity-induced bunch lengthening is considered, the harmonic cavity is introduced through the `RFMODE` element, with its frequency, shunt impedance (R), and quality factor (Q) set consistently with those used in `STABLE`. The long-range transverse RW wakefield is modeled using a single `LRWAKE` element, and the history retention length is adjusted according to the tracking condition. To monitor the multibunch evolution, one `WATCH` element is assigned to each rf bucket to record the turn-by-turn bunch centroids, from which the coupled-bunch mode growth rates are extracted.

[1] W. Li, T. He, and Z. Bai, Terahertz scale microbunching instability driven by high resistivity nonevaporable getter coating resistive-wall impedance, Phys. Rev. Accel. Beams **27**, 034401 (2024).

[2] L. R. Carver, T. Brochard, E. Buratin, N. Carmignani, F. Ewald, L. Hoummi, S. M. Liuzzo, T. Perron, B. Roche, and S. White, Beam based characterization of the European synchrotron radiation facility extremely brilliant source short range wakefield model, Phys. Rev. Accel. Beams **26**, 044402 (2023).

[3] V. Gubaidulin, A. Gamelin, A. Loulergue, R. Nagaoka, and P. Schreiber, Transverse instabilities in SOLEIL II storage ring in the presence of a harmonic cavity, in *Proc. IPAC'24, Nashville, TN, USA* (JACoW Publishing, Geneva, Switzerland, 2024), pp. 821–824, MOPS45.

[4] F. J. Cullinan, R. Nagaoka, G. Skripka, and P. F. Tavares, Transverse coupled-bunch instability thresholds in the presence of a harmonic-cavity-flattened rf potential, Phys. Rev. Accel. Beams **19**, 124401 (2016).

[5] S. Dastan, E. Karantzoulis, K. Manukyan, S. Krecic, and R. Nagaoka, Study on transverse multi-bunch instability in Elettra 2.0, in *Proc. IPAC'23, Venice, Italy* (JACoW Publishing, Geneva, Switzerland, 2023), pp. 1106–1109, MOPM050.

[6] N. Wang, J. T. Li, S. K. Tian, S. Yue, and X. Y. Liu, Narrowband impedance studies in the HEPS storage ring, in *Proc. IPAC'24, Nashville, TN, USA* (JACoW Publishing, Geneva, Switzerland, 2024), pp. 3144–3147, THPC58.

[7] S. W. Wang, H. C. Chao, R. T. Fielder, I. P. S. Martin, and T. Olsson, Studies of transverse coupled-bunch instabilities from resistive-wall and cavity higher order modes for Diamond-II, in *Proc. IPAC'22, Bangkok, Thailand* (JACoW Publishing, Geneva, Switzerland, 2022), pp. 2253–2256, WEPOMS010.

[8] X. Ai *et al.*, Conceptual design report of the Super Tau-Charm Facility: The accelerator, Nucl. Sci. Tech. **36**, 242 (2025).

[9] E. Belli, M. Migliorati, G. Castorina, B. Spataro, M. Zobov, A. Novokhatski, and S. Persichelli, Coupling impedances and collective effects for FCC-ee, in *Proc. IPAC'17, Copenhagen, Denmark* (JACoW Publishing, Geneva, Switzerland, 2017), pp. 3734–3737, THPAB020.

[10] N. Wang, C. T. Lin, Y. D. Liu, S. K. Tian, H. S. Xu, and Y. Zhang, Collective effects studies for CEPC, in *Proc. eeFACT'22, Frascati, Italy* (JACoW Publishing, Geneva, Switzerland, 2022), pp. 141–145, WEYAT0101.

[11] D. Zhou, M. Tobiyama, G. Mitsuka, T. Ishibashi, and M. Migliorati, Transverse coupled-bunch instability driven by the resistive wall impedance at SuperKEKB, in *Proc. IPAC'23, Venice, Italy* (JACoW Publishing, Geneva, Switzerland, 2023), pp. 3562–3565, WEPL187.

[12] N. Mounet, The LHC Transverse Coupled-Bunch Instability, Ph.D. thesis, EPFL, Lausanne, 2012.

[13] S. Persichelli, M. Migliorati, N. Biancacci, S. Gilardoni, E. Metral, and B. Salvant, Transverse beam coupling impedance of the CERN proton synchrotron, Phys. Rev. Accel. Beams **19**, 041001 (2016).

[14] A. W. Chao, *Physics of Collective Beam Instabilities in High Energy Accelerators* (Wiley, New York, 1993), https://books.google.com.hk/books?id=MjRoQgAACAAJ.

[15] F. J. Sacherer, Transverse bunched beam instabilities: Theory, in *Proc. HEACC'74, Stanford, CA, USA* (A.E.C., Washington, DC, 1975), pp. 347–351, https://cds.cern.ch/record/322645.

[16] J. L. Laclare, Bunched beam coherent instabilities, in *CAS–CERN Accelerator School: Accelerator Physics, Oxford, UK, 16-25 September 1985*, edited by S. Turner (CERN, Geneva, Switzerland, 1987), pp. 264–326.

[17] G. Bassi, A. Blednykh, and V. Smaluk, Coupled-bunch instability for arbitrary multibunch configurations, Phys. Rev. Accel. Beams **25**, 014402 (2022).

[18] R. R. Lindberg, Stabilizing effects of chromaticity and synchrotron emission on coupled-bunch transverse dynamics in storage rings, Phys. Rev. Accel. Beams **24**, 024402 (2021).

[19] F. J. Cullinan, Å. Andersson, and P. F. Tavares, Harmonic-cavity stabilization of longitudinal coupled-bunch instabilities with a nonuniform fill, Phys. Rev. Accel. Beams **23**, 074402 (2020).

[20] M. Borland, ELEGANT: A flexible SDDS-compliant code for accelerator simulation, Tech. Rep., Argonne National Lab., IL, USA, 2000.

[21] Y. Wang and M. Borland, Pelegant: A parallel accelerator simulation code for electron generation and tracking, in *AIP Conference Proceedings* (AIP, Melville, NY, 2006), pp. 241–247.

[22] A. Gamelin, W. Foosang, and R. Nagaoka, mbtrack2, a collective effect library in Python, in *Proc. IPAC'21, Campinas, SP, Brazil* (JACoW Publishing, Geneva, Switzerland, 2021), pp. 282–285, MOPAB070.

[23] A. Gamelin, W. Foosang, N. Yamamoto, V. Gubaidulin, and R. Nagaoka, mbtrack2 (Version 0.10.0), Zenodo, 10.5281/zenodo.20607804 (2026).

[24] G. Iadarola *et al.*, Xsuite: An integrated beam physics simulation framework, in *Proc. IPAC'24, Nashville, TN, USA* (JACoW Publishing, Geneva, Switzerland, 2024), pp. 2623–2626, WEPR56.

[25] Xsuite Collaboration, xsuite/xtrack:Xtrack version 0.111.5, Zenodo, 10.5281/zenodo.22040751 (2026).

[26] C. Li and Y.-C. Chae, CETASim: A numerical tool for beam collective effect study in storage rings, Nucl. Instrum. Methods Phys. Res., Sect. A **1070**, 170031 (2025).

[27] M. Migliorati and L. Palumbo, Multibunch and multiparticle simulation code with an alternative approach to wakefield effects, Phys. Rev. ST Accel. Beams **18**, 031001 (2015).

[28] T. He and Z. Bai, Graphics-processing-unit-accelerated simulation for longitudinal beam dynamics of arbitrary bunch trains in electron storage rings, Phys. Rev. Accel. Beams **24**, 104401 (2021).

[29] W. W. Li, Y. Sun, X. Y. Liu, T. L. He, and Z. H. Bai, Study on transverse coupled-bunch instabilities driven by high order modes in the HALF storage ring, Nucl. Instrum. Methods Phys. Res., Sect. A **1083**, 171104 (2026).

[30] Z. Bai *et al.*, Progress on the storage ring physics design of Hefei Advanced Light Facility (HALF), in *Proc. IPAC'23, Venice, Italy* (JACoW Publishing, Geneva, Switzerland, 2023), pp. 1075–1078, MOPM038.

[31] Y. Shobuda and Y. H. Chin, Resistive-wall impedances of a thin non-evaporable getter coating on a conductive chamber, Prog. Theor. Exp. Phys. **2017**, 123G01 (2017).

[32] A. Blednykh, G. Bassi, V. Smaluk, and R. Lindberg, Impedance modeling and its application to the analysis of the collective effects, Phys. Rev. Accel. Beams **24**, 104801 (2021).

[33] J. Kennedy and R. Eberhart, Particle swarm optimization, in *Proc. ICNN'95–International Conference on Neural Networks* (IEEE, New York, 1995), Vol. 4, pp. 1942–1948.

[34] S. Katoch, S. S. Chauhan, and V. Kumar, A review on genetic algorithm: Past, present, and future, Multimedia Tools Appl. **80**, 8091 (2021).

[35] P. I. Frazier, Bayesian optimization, in *Recent Advances in Optimization and Modeling of Contemporary Problems* (INFORMS, Catonsville, MD, 2018), pp. 255–278.

[36] J. Blank and K. Deb, Pymoo: Multi-objective optimization in Python, IEEE Access **8**, 89497 (2020).

[37] W. McLean, Exponential sum approximations for $t^{-\beta}$, in *Contemporary Computational Mathematics–A Celebration of the 80th Birthday of Ian Sloan*, edited by J. Dick, F. Y. Kuo, and H. Woźniakowski (Springer International Publishing, Cham, 2018), pp. 911–930.

[38] X. Huang, H. Yao, T. He, W. Li, X. Liu, Z. Bai, and H. Xu, Exponential sum fitting of the long-range transverse resistive-wall wakefield, in *Proc. SAP'25, Urumqi, China* (JACoW Publishing, Geneva, Switzerland, 2025), pp. 61–64, THP22.

[39] T. He, W. Li, Z. Bai, and L. Wang, Periodic transient beam loading effect with passive harmonic cavities in electron storage rings, Phys. Rev. Accel. Beams **25**, 024401 (2022).

[40] T. He, W. Li, Z. Bai, and W. Li, Analytic formulas for the *D*-mode Robinson instability, Phys. Rev. Accel. Beams **27**, 064402 (2024).

[41] R. Nagaoka and K. L. F. Bane, Collective effects in a diffraction-limited storage ring, J. Synchrotron Radiat. **21**, 937 (2014).

[42] T. He, W. Li, Z. Bai, and L. Wang, Longitudinal equilibrium density distribution of arbitrary filled bunches in

presence of a passive harmonic cavity and the short range wakefield, Phys. Rev. Accel. Beams **24**, 044401 (2021).

[43] A. Poncet, Ion trapping and clearing, in *Frontiers of Particle Beams: Factories with e+e- Rings* (Springer, Berlin, Heidelberg, 1994), pp. 202–221.

[44] K. Holldack, R. Ovsyannikov, P. Kuske, R. Müller, A. Schälicke, M. Scheer, M. Gorgoi, D. Kühn, T. Leitner, S. Svensson, N. Mårtensson, and A. Föhlisch, Single bunch X-ray pulses on demand from a multi-bunch synchrotron radiation source, Nat. Commun. **5**, 4010 (2014).

[45] Z. T. Zhao, Y. N. Liang, and B. C. Jiang, Filling patterns in the SSRF storage ring, Nucl. Sci. Tech. **21**, 129 (2010).

[46] R. Warnock and M. Venturini, Equilibrium of an arbitrary bunch train in presence of a passive harmonic cavity: Solution through coupled Haïssinski equations, Phys. Rev. Accel. Beams **23**, 064403 (2020).

[47] T. Olsson, F. J. Cullinan, and Å. Andersson, Self-consistent calculation of transient beam loading in electron storage rings with passive harmonic cavities, Phys. Rev. Accel. Beams **21**, 120701 (2018).

[48] L. Wang, Y. Cai, T. O. Raubenheimer, and H. Fukuma, Suppression of beam-ion instability in electron rings with multibunch train beam fillings, Phys. Rev. ST Accel. Beams **14**, 084401 (2011).

[49] V. Gubaidulin, A. Gamelin, and R. Nagaoka, Beam-ion instabilities and their mitigation for SOLEIL II, in *Proc. IPAC'23, Venice, Italy* (JACoW Publishing, Geneva, Switzerland, 2023), pp. 2650–2653, WEPA004.

[50] M. Dehler, Ion trapping and instabilities in SLS 2.0, in *Proc. IPAC'23, Venice, Italy* (JACoW Publishing, Geneva, Switzerland, 2023), pp. 3578–3581, WEPL192.

[51] S. Prabhakar, J. D. Fox, and D. Teytelman, Curing coupled-bunch instabilities with uneven fills, Phys. Rev. Lett. **86**, 2022 (2001).

[52] R. Roussel *et al.*, Bayesian optimization algorithms for accelerator physics, Phys. Rev. Accel. Beams **27**, 084801 (2024).

[53] T. Hellert, D. Bertwistle, S. C. Leemann, A. Sulc, and M. Venturini, Agentic artificial intelligence for multistage physics experiments at a large-scale user facility particle accelerator, Phys. Rev. Res. **8**, L012017 (2026).

[54] N. Mounet, N. Biancacci, D. Amorim, and E. Vik, ImpedanceWake2D, CERN GitLab repository, https://gitlab.cern.ch/IRIS/IW2D.

[55] K. Yokoya, Resistive wall impedance of beam pipes of general cross-section, Part. Accel. **41**, 221 (1993). https://api.semanticscholar.org/CorpusID:34843045

[56] G. Bassi, A. Blednykh, W. Cheng, F. Gao, J. Rose, and D. Teytelman, Analysis of coupled-bunch instabilities for the NSLS-II storage ring with a 500 MHz 7-cell PETRA-III cavity, Nucl. Instrum. Methods Phys. Res., Sect. A **810**, 151 (2016).

[57] T. L. He, J. C. Xiao, W. W. Li, Z. H. Bai, and W. M. Li, Impact of short-range wakefields from radio-frequency cavity resonant modes on bunch lengthening, Nucl. Instrum. Methods Phys. Res. Sect. A **1080**, 170672 (2025).